intracellular proteins, resulting in C-terminal fragments that often bear destabilizing N-terminal residues of the Ubr1-mediated branch of the N-end–rule pathway (fig. S1C). Such fragments are often short-lived in vivo, thereby regulating specific circuits [reviewed in (*13*)]. Given the major expansion of the N-end rule in the present work (Fig. 4), most in vivo–produced C-terminal fragments of intracellular proteins should now be viewed, a priori, as putative targets of the Doa10 or Ubr1 branches of the N-end–rule pathway.

The topologically unique location of N-terminal residues, their massive involvement in proteolysis, and their extensive modifications make N-degrons a particularly striking example of the scope and subtlety of regulated protein degradation (Fig. 4 and fig. S1C).

References and Notes

1. H. Jörnvall, *J. Theor. Biol.* **55**, 1 (1975).
2. J. R. Mullen *et al.*, *EMBO J.* **8**, 2067 (1989).
3. E. C. Park, J. W. Szostak, *EMBO J.* **11**, 2087 (1992).
4. M. Gautschi *et al.*, *Mol. Cell. Biol.* **23**, 7403 (2003).
5. B. Polevoda, F. Sherman, *J. Mol. Biol.* **325**, 595 (2003).
6. T. Arnesen *et al.*, *Proc. Natl. Acad. Sci. U.S.A.* **106**, 8157 (2009).
7. S. Goetze *et al.*, *PLoS Biol.* **7**, e1000236 (2009).
8. F. Frottin *et al.*, *Mol. Cell. Proteomics* **5**, 2336 (2006).
9. A. Mayer, N. R. Siegel, A. L. Schwartz, A. Ciechanover, *Science* **244**, 1480 (1989).
10. A. Bachmair, D. Finley, A. Varshavsky, *Science* **234**, 179 (1986).
11. A. Bachmair, A. Varshavsky, *Cell* **56**, 1019 (1989).
12. A. Varshavsky, *Proc. Natl. Acad. Sci. U.S.A.* **93**, 12142 (1996).
13. A. Varshavsky, *J. Biol. Chem.* **283**, 34469 (2008).
14. A. Mogk, R. Schmidt, B. Bukau, *Trends Cell Biol.* **17**, 165 (2007).
15. T. Tasaki, Y. T. Kwon, *Trends Biochem. Sci.* **32**, 520 (2007).
16. R.-G. Hu *et al.*, *Nature* **437**, 981 (2005).
17. R.-G. Hu, H. Wang, Z. Xia, A. Varshavsky, *Proc. Natl. Acad. Sci. U.S.A.* **105**, 76 (2008).
18. C.-S. Hwang, A. Varshavsky, *Proc. Natl. Acad. Sci. U.S.A.* **105**, 19188 (2008).
19. C.-S. Hwang, A. Shemorry, A. Varshavsky, *Proc. Natl. Acad. Sci. U.S.A.* **106**, 2142 (2009).
20. H. Wang, K. I. Piatkov, C. S. Brower, A. Varshavsky, *Mol. Cell* **34**, 686 (2009).
21. A. Varshavsky, *Methods Enzymol.* **399**, 777 (2005).
22. R. Swanson, M. Locher, M. Hochstrasser, *Genes Dev.* **15**, 2660 (2001).
23. M. Deng, M. Hochstrasser, *Nature* **443**, 827 (2006).
24. T. Ravid, S. G. Kreft, M. Hochstrasser, *EMBO J.* **25**, 533 (2006).
25. M. Hochstrasser, A. Varshavsky, *Cell* **61**, 697 (1990).
26. P. Chen, P. Johnson, T. Sommer, S. Jentsch, M. Hochstrasser, *Cell* **74**, 357 (1993).
27. A. D. Johnson, *Curr. Opin. Genet. Dev.* **5**, 552 (1995).
28. O. A. Zill, J. Rine, *Genes Dev.* **22**, 1704 (2008).
29. Single-letter abbreviations for the amino acid residues are as follows: A, Ala; C, Cys; D, Asp; E, Glu; F, Phe; G, Gly; H, His; I, Ile; K, Lys; L, Leu; M, Met; N, Asn; P, Pro; Q, Gln; R, Arg; S, Ser; T, Thr; V, Val; W, Trp; and Y, Tyr.
30. Materials and methods are available as supporting material on *Science* Online.
31. G. Hassink *et al.*, *Biochem. J.* **388**, 647 (2005).

32. We thank J. Zhou (Caltech) for MS analyses and C. Brower for comments on the paper. We are grateful to members of the Varshavsky laboratory for their advice in the course of this study and particularly thank O. Batygin for her technical assistance. This work was supported by grants from NIH and the March of Dimes Foundation to A.V.

Supporting Online Material

www.sciencemag.org/cgi/content/full/science.1183147/DC1
Materials and Methods
SOM Text
Figs. S1 to S9
Tables S1 to S3
References

9 October 2009; accepted 12 January 2010
Published online 28 January 2010;
10.1126/science.1183147
Include this information when citing this paper.

Kepler Planet-Detection Mission: Introduction and First Results

William J. Borucki,[1]* David Koch,[1] Gibor Basri,[2] Natalie Batalha,[3] Timothy Brown,[4] Douglas Caldwell,[5] John Caldwell,[17] Jørgen Christensen-Dalsgaard,[6] William D. Cochran,[7] Edna DeVore,[5] Edward W. Dunham,[8] Andrea K. Dupree,[10] Thomas N. Gautier III,[9] John C. Geary,[10] Ronald Gilliland,[11] Alan Gould,[18] Steve B. Howell,[15] Jon M. Jenkins,[5] Yoji Kondo,[29] David W. Latham,[10] Geoffrey W. Marcy,[2] Søren Meibom,[10] Hans Kjeldsen,[6] Jack J. Lissauer,[1] David G. Monet,[12] David Morrison,[1] Dimitar Sasselov,[10] Jill Tarter,[5] Alan Boss,[19] Don Brownlee,[21] Toby Owen,[20] Derek Buzasi,[22] David Charbonneau,[10] Laurance Doyle,[5] Jonathan Fortney,[24] Eric B. Ford,[13] Matthew J. Holman,[10] Sara Seager,[25] Jason H. Steffen,[26] William F. Welsh,[27] Jason Rowe,[1] Howard Anderson,[2] Lars Buchhave,[10] David Ciardi,[28] Lucianne Walkowicz,[2] William Sherry,[15] Elliott Horch,[23] Howard Isaacson,[2] Mark E. Everett,[14] Debra Fischer,[16] Guillermo Torres,[10] John Asher Johnson,[28] Michael Endl,[7] Phillip MacQueen,[7] Stephen T. Bryson,[1] Jessie Dotson,[1] Michael Haas,[1] Jeffrey Kolodziejczak,[30] Jeffrey Van Cleve,[5] Hema Chandrasekaran,[5] Joseph D. Twicken,[5] Elisa V. Quintana,[5] Bruce D. Clarke,[5] Christopher Allen,[31] Jie Li,[5] Haley Wu,[5] Peter Tenenbaum,[5] Ekaterina Verner,[32] Frederick Bruhweiler,[32] Jason Barnes,[33] Andrej Prsa[34]

The Kepler mission was designed to determine the frequency of Earth-sized planets in and near the habitable zone of Sun-like stars. The habitable zone is the region where planetary temperatures are suitable for water to exist on a planet's surface. During the first 6 weeks of observations, Kepler monitored 156,000 stars, and five new exoplanets with sizes between 0.37 and 1.6 Jupiter radii and orbital periods from 3.2 to 4.9 days were discovered. The density of the Neptune-sized Kepler-4b is similar to that of Neptune and GJ 436b, even though the irradiation level is 800,000 times higher. Kepler-7b is one of the lowest-density planets (~0.17 gram per cubic centimeter) yet detected. Kepler-5b, -6b, and -8b confirm the existence of planets with densities lower than those predicted for gas giant planets.

Since the first discoveries of planetary companions around pulsars (*1*, *2*) and normal stars (*3*), more than 400 such planets have been detected. Most of these are giant planets, often more massive than Jupiter. Many have a semimajor axis (mean star/planet separation) of less than 1 astronomical unit (AU, the distance between Earth and the Sun) and/or high eccentricity. These surprisingly small semimajor axes suggest that many planets form at

[1]NASA Ames Research Center, Moffett Field, CA 94035, USA. [2]University of California, Berkeley, CA 94720, USA. [3]San Jose State University, San Jose, CA 95192, USA. [4]Las Cumbres Observatory Global Telescope, Goleta, CA 93117, USA. [5]SETI Institute, Mountain View, CA 94043, USA. [6]Aarhus University, Aarhus, Denmark. [7]McDonald Observatory, University of Texas at Austin, Austin, TX 78712, USA. [8]Lowell Observatory, Flagstaff, AZ 86001, USA. [9]Jet Propulsion Laboratory, California Institute of Technology, Pasadena, CA 91109, USA. [10]Harvard-Smithsonian Center for Astrophysics, Cambridge, MA 02138, USA. [11]Space Telescope Science Institute, Baltimore, MD 21218, USA. [12]United States Naval Observatory, Flagstaff, AZ 86001, USA. [13]University of Florida, Gainesville, FL 32611, USA. [14]Planetary Science Institute, Tucson, AZ 85719, USA. [15]National Optical Astronomy Observatory, Tucson, AZ 85719, USA. [16]Yale University, New Haven, CT 06520, USA. [17]York University, North York, M3J 1P3 Ontario, Canada. [18]Lawrence Hall of Science, Berkeley, CA 94720, USA. [19]Carnegie Institute of Washington, Washington, DC 20015 USA. [20]University of Hawaii, Hilo, HI 96720 USA. [21]University of Washington, Seattle, WA 98195, USA. [22]Eureka Scientific, Oakland, CA 94602, USA. [23]Southern Connecticut State University, New Haven, CT 06515, USA. [24]University of California, Santa Cruz, CA 95064, USA. [25]Massachusetts Institute of Technology, Cambridge, MA 02139, USA. [26]Fermilab, Batavia, IL 60510, USA. [27]San Diego State University, San Diego, CA 92182, USA. [28]Exoplanet Science Institute/Caltech, Pasadena, CA 91125, USA. [29]NASA Goddard Space Flight Center, Greenbelt, MD 20025, USA. [30]Marshall Space Flight Center, Huntsville, AL 35805, USA. [31]Orbital Sciences, Mountain View, CA 94043, USA. [32]Catholic University of America, Washington, DC 20064, USA. [33]University of Idaho, Moscow, ID 83844, USA. [34]Villanova University, Villanova, PA 19085, USA.

*To whom correspondence should be addressed. E-mail: William.J.Borucki@nasa.gov

several astronomical units from their stars before migrating to their current locations. The processes that terminate the inward migration and the fraction of planets that fall into their stars are not known. Although the inward migration of a giant planet is expected to remove inner, smaller planets by scattering them into the star or out of the planetary system, a second generation of planets might reaccrete in the wake of the migrating planet (*4*). Because it is difficult to predict or detect terrestrial planets, their frequency and distributions are unknown.

Kepler includes a differential photometer with a wide (115 square degrees) field of view (FOV) that continuously and simultaneously monitors the brightness of approximately 150,000 main-sequence stars. The photometer is based on a modified Schmidt telescope design that uses a corrector with a 0.95-m aperture and a 1.4-m diameter *f*/1 primary mirror. The aperture is sufficient to reduce the Poisson noise to the level that is required to obtain a 4σ detection for a single transit from an Earth-sized planet passing in front of a 12th-magnitude G2 dwarf (that is, a Sun-like star) with a 6.5-hour transit. The mission was launched on 6 March 2009 into an Earth-trailing orbit. Its design, characteristics, selection of target stars, on-orbit performance, data processing pipeline, data characteristics, and mission operations can be found in the supporting online material (SOM) text, section 1, and (*5*–*11*).

Here we describe the detection of five new exoplanets of varying size and orbital period based on the first two data segments taken at the start of the mission, and we provide some comparisons with previous detections. The first segment is a 9.7-day period (Q0) starting on 2 May 2009 universal time (UT) during the commissioning phase. The second is a 33.5-day period (Q1) taken at the beginning of science operations on 13 May 2009 UT. For Q0, oversized apertures were used to image each star, because the point-spread function and geometry of the focal plane were not yet known precisely. During this period, nearly all stars brighter than $V = 13.6$ magnitude in the FOV were observed (52,496 in total). Analysis of these data sets also led to a series of astrophysical discoveries, including oscillations of giant stars and two examples of planet-sized objects that are hotter than the stars they orbit (*12*–*21*).

The Q1 observations used smaller apertures, which allowed 156,097 objects to be observed. Targets were chosen to maximize the number of stars that were both bright and small enough to show detectable transit signals for small planets in and near the habitable zone (HZ) [SOM text 2 (*11*)].

Planets orbiting close to hot stars can reach temperatures in excess of 2000 K and can emit enough light for Kepler to detect their thermal radiation in the range of visible wavelengths. Kepler's first observations detected thermal emission from exoplanet HAT-P-7b (*22*, *23*). The phase curve of the emission provided information about the planetary albedo, the depth of absorption in the planet's atmosphere, and the lack of redistribution of the energy to the night side of the planet. Analysis of the first data set led to the discovery of ellipsoidal variations in the host star (*24*).

Several planetary candidates that passed the tests to remove false-positive events (SOM text 3) were observed with radial velocity (RV) spectrometers to determine their masses. (See SOM text 4 for the approach used to determine the characteristics of the planets from the observations.) Modeling was performed to establish the system characteristics and uncertainties (*25*). Each target has a Kepler identification number (KIC no.) from the Kepler Input Catalog (KIC), but each confirmed exoplanet is also assigned a convenient abbreviation (Kepler-number-letter) (Tables 1 and 2). The numbering begins with 4b, because the designations 1b, 2b, and 3b are used to refer to previously known exoplanets in the Kepler FOV: TrES-2 (*26*), HAT-P-7b (*22*), and HAT-P-11b (*27*), respectively.

Table 1. Properties of the exoplanets detected by Kepler. The state of the current observations is insufficient to support claims of nonzero eccentricity. Therefore, parameter estimates are based on the assumption of a circular orbit. Calculations of the equilibrium temperatures assume a Bond albedo = 0.1 and efficient transport of heat to the night side. Epoch = HJD-2454900.0. R_J is the Jupiter equatorial radius. M_J is the mass of Jupiter. Errors are ± 1σ and represent formal errors only.

Identification	KIC no.	Period (days)	Epoch	Radius (R_J)	Mass (M_J)	Density (g/cm^3)	Equilibrium temperature (K)	Semimajor axis (AU)	Inclination (degrees)	Reference
Kepler-4b	11853905	3.21346 ± 0.00022	56.6127 ± 0.0015	0.357 ± 0.021	0.077 ± 0.012	1.91 ± 0.41	1650 ± 200	0.04558 ± 0.00087	89.76 ± 1.17	(*25*)
Kepler-5b	8191672	3.548460 ± 0.000032	55.90122 ± 0.00021	1.431 ± 0.048	2.114 ± 0.064	0.894 ± 0.079	1868 ± 284	0.05064 ± 0.00070	86.3 ± 0.6	(*30*)
Kepler-6b	10874614	3.234723 ± 0.000017	54.48636 ± 0.00014	1.323 ± 0.026	0.669 ± 0.027	0.352 ± 0.019	1500 ± 200	0.04567 ± 0.00050	86.8 ± 0.3	(*29*)
Kepler-7b	5780885	4.885525 ± 0.000039	67.27567 ± 0.00014	1.478 ± 0.051	0.433 ± 0.040	0.166 ± 0.019	1540 ± 200	0.06224 ± 0.00127	86.5 ± 0.4	(*28*)
Kepler-8b	6922244	3.52254 ± 0.00004	54.1182 ± 0.0003	1.419 ± 0.055	0.603 ± 0.154	0.261 ± 0.071	1764 ± 200	0.0483 ± 0.0008	84.07 ± 0.33	(*31*)

Table 2. Characteristics of the stars hosting Kepler planets. *Kp* is the stellar magnitude calculated for the Kepler band pass. The values are similar to those produced by an R filter (*7*) for most star types. Right ascension (RA) and declination (dec) refer to the J2000.0 equinox. For three of the stars (Kepler-4, -5, and -7), the model fits give two peaks in the distributions of the mass and radius. The values listed here are thought to be the best estimate (*25*, *28*–*31*). log(*g*) values are calculated from model fit based on stellar density and temperature. T_{eff} , effective temperature. M^* and R^* are the mass and radius of the host stars, respectively. M_{Sun} and R_{Sun} are the mass and radius of the Sun, respectively.

Identification	M^* (M_{Sun})	R^* (R_{Sun})	log(*g*) (cgs)	[Fe/H]	T_{eff} (K)	*Kp* (mag)	RA, dec (hour, degree)
Kepler-4	1.223 ± 0.068	1.487 ± 0.084	4.165 ± 0.037	0.17 ± 0.06	5857 ± 60	12.21	19.04102, 50.13575
Kepler-5	1.374 ± 0.056	1.793 ± 0.053	4.067 ± 0.020	0.04 ± 0.06	6297 ± 60	13.4	19.96047, 44.03505
Kepler-6	1.209 ± 0.040	1.391 ± 0.024	4.236 ± 0.011	0.34 ± 0.06	5647 ± 44	13.3	19.78915, 48.23994
Kepler-7	1.347 ± 0.080	1.843 ± 0.057	4.030 ± 0.018	0.11 ± 0.03	5933 ± 44	12.9	19.23877, 41.08981
Kepler-8	1.213 ± 0.063	1.486 ± 0.056	4.174 ± 0.026	-0.055 ± 0.033	6213 ± 75	13.6	18.75254, 42.45108

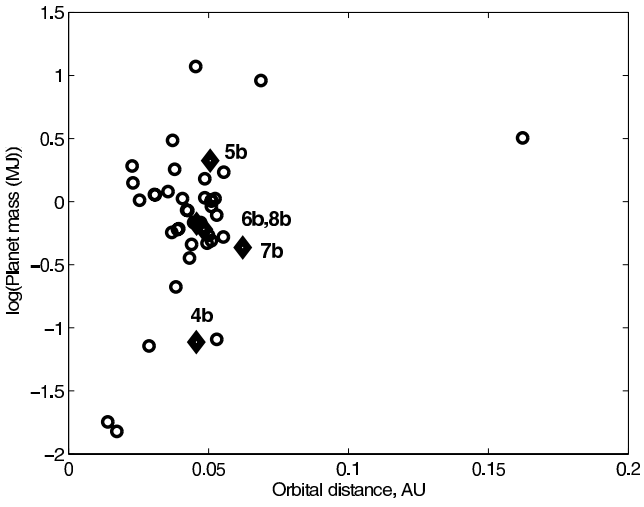

Fig. 1. Comparison of mass versus semimajor axes for Kepler planets. Circles represent transiting planets listed in the Extrasolar Planets Encyclopedia (*37*).

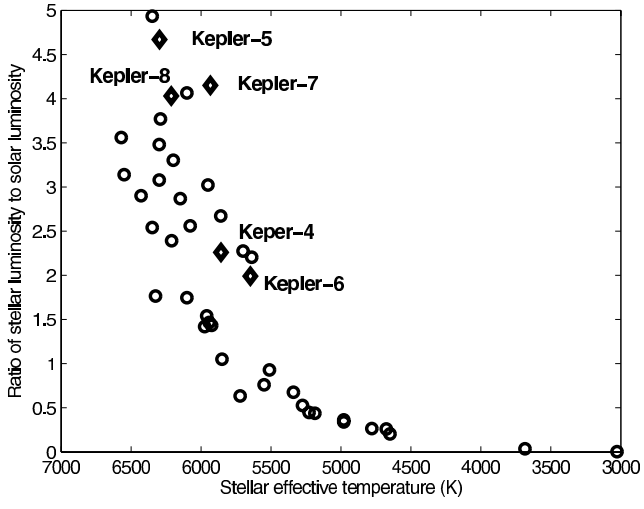

Fig. 2. Comparison of stars associated with the Kepler exoplanets with those associated with the planets in the Extrasolar Planet Encyclopedia. The parameter plotted on the vertical axis is the ratio of the area of the star multiplied by its effective temperature to the fourth power divided by solar values.

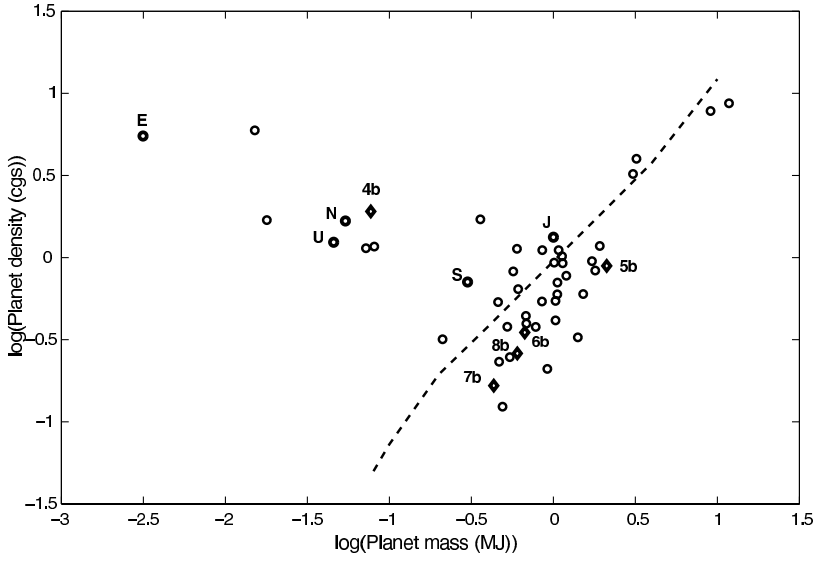

Fig. 3. Planet density versus mass. Kepler planets are shown as diamonds. Letter symbols represent solar system planets. Placement of the Kepler exoplanets on mass-radius diagrams can be found in (*25*, *28*). Circles represent transiting planets listed in the Extrasolar Planet Encyclopedia. The data to the right show planet density increasing with mass. The dashed line is the prediction for planets composed only of H and He and receiving irradiation associated with a Sun-like star at a distance of 0.045 AU (*34*). Rocky planets similar to Earth without atmospheres that contribute substantially to the mass of the planet are at the left. In between are ice giants, which are mixtures of H/He and rocky material (*36*).

Light curves and RV curves can be found in SOM text 5 and (*25*, *28*–*31*). The results presented in the Tables 1 and 2 are based on time series of photometry and radial velocity data that can be retrieved from the Space Telescope Science Institute's Multimission Archive at STScI/high-level science products (MAST/HLSP) data archive (*32*).

Kepler-4b is an exoplanet that is very similar in size, density, and mass to Neptune (the most probable estimates are 1.03 times the size, 1.09 times the density, and 1.43 times the mass) and is similar in mass and radius to GJ 436b (*33*). A major difference between Kepler-4b and Neptune is that the irradiance level for Kepler-4b is over 800,000 times larger than that of Neptune. However, the large difference in irradiance levels appears to make little difference to the sizes of the planets. The result implies a difference in bulk composition (*34*), with either a higher rock-to-water ratio or less H/He in Kepler-4b as compared with Neptune (and GJ 436b). The latter degeneracy cannot be resolved at this time.

The Kepler results did not find planets with very small values of semimajor axes (Fig. 1), even though such planets would have a larger probability of alignment than those with larger values. The stars associated with the Kepler exoplanets are generally larger than those shown in the Exoplanet Encyclopedia for transiting planets (Fig. 2). The difference could be due to the Malmquist bias or to the preferential selection of stars with sharp spectral lines for the Kepler follow-up; that is, slightly evolved stars.

The data add to the evidence for three planet populations (Fig. 3) and the separation between ice giants and gas giants. The scatter in the data might be explained by differing fractions of heavy elements and H/He envelopes (*35*, *36*). However, it is surprising that Kepler exoplanets 5b, 6b, 7b, and 8b, as well as many other transiting planets shown in Fig. 3, also lie below the curve for a pure H/He planet (*34*). The radii of Uranus, Neptune, GJ 436b, HAT-P-11b, and Kepler-4b have been shown to lie below the predicted irradiated and nonirradiated radius-mass curves (*25*, *35*).

References and Notes

1. A. Wolszczan, D. A. Frail, *Nature* **355**, 145 (1992).
2. A. Wolszczan, *Science* **264**, 538 (1994).
3. M. Mayor, D. Queloz, *Nature* **378**, 355 (1995).
4. S. N. Raymond, A. M. Mandell, S. Sigurdsson, *Science* **313**, 1413 (2006).
5. D. Koch *et al.*, *Astrophys. J.*, preprint available at http://xxx.lanl.gov/abs/1001.0268.
6. W. J. Borucki *et al.*, *Proc. IAU Symp.* **253**, 289 (2008).
7. R. L. Gilliland *et al.*, *Astrophys. J.*, preprint available at http://xxx.lanl.gov/abs/1001.0142.
8. D. A. Caldwell *et al.*, *Astrophys. J.*, preprint available at http://xxx.lanl.gov/abs/1001.0216.
9. J. M. Jenkins *et al.*, *Astrophys. J.*, preprint available at http://xxx.lanl.gov/abs/1001.0256.
10. M. R. Haas *et al.*, *Astrophys. J.*, preprint available at http://xxx.lanl.gov/abs/1001.0437.
11. N. M. Batalha *et al.*, *Astrophys. J.*, preprint available at http://xxx.lanl.gov/abs/1001.0349.

12. R. L. Gilliland *et al.*, *Publ. Atron. Soc. Pacific*, preprint available at http://xxx.lanl.gov/abs/1001.0139.
13. J. Christensen-Dalsgaard *et al.*, *Astrophys. J.*, preprint available at http://xxx.lanl.gov/abs/1001.0032.
14. W. J. Chaplin *et al.*, *Astrophys. J.*, preprint available at http://xxx.lanl.gov/abs/1001.0506.
15. G. Basri *et al.*, *Astrophys. J.*, preprint available at http://xxx.lanl.gov/abs/1001.0414.
16. D. Stello *et al.*, *Astrophys. J.*, preprint available at http://xxx.lanl.gov/abs/1001.0026.
17. T. R. Bedding *et al.*, *Astrophys. J.*, preprint available at http://xxx.lanl.gov/abs/1001.0229.
18. S. Hekker *et al.*, *Astrophys. J.*, preprint available at http://xxx.lanl.gov/abs/1001.0399.
19. K. Kolenberg *et al.*, *Astrophys. J.*, preprint available at http://xxx.lanl.gov/abs/1001.0417.
20. A. Grigachcene *et al.*, *Astrophys. J.*, preprint available at http://xxx.lanl.gov./1001.0747.
21. J. F. Rowe *et al.*, *Astrophys. J.*, preprint available at http://xxx.lanl.gov/abs/1001.3420.
22. A. Pál *et al.*, *Astrophys. J.* **680**, 1450 (2008).
23. W. J. Borucki *et al.*, *Science* **325**, 709 (2009).
24. W. F. Welsh *et al.*, *Astrophys. J.*, preprint available at http://xxx.lanl.gov/abs/1001.0413.
25. W. J. Borucki *et al.*, *Astrophys. J.*, preprint available at http://xxx.lanl.gov/abs/1001.0604v1.
26. F. T. O'Donovan *et al.*, *Astrophys. J.* **651**, L61 (2006).
27. G. A. Bakos *et al.*, *Astrophys. J.*, preprint available at http://xxx.lanl.gov/abs/0901.0282.
28. D. W. Latham *et al.*, *Astrophys. J.*, preprint available at http://xxx.lanl.gov/abs/1001.0190.
29. E. W. Dunham *et al.*, *Astrophys. J.*, preprint available at http://xxx.lanl.gov/abs/1001.0333.
30. D. G. Koch *et al.*, *Astrophys. J.*, preprint available at http://xxx.lanl.gov./abs/1001.0913.
31. J. M. Jenkins *et al.*, *Astrophys. J.*, preprint available at http://xxx.lanl.gov/abs/1001.0416.
32. The MAST/HLSP data archive is available at http://archive.stsci.edu/prepds/kepler_hlsp.
33. M. Gillon *et al.*, *Astron. Astrophys.* **472**, L13 (2007).
34. J. J. Fortney, in *ASP Conference Series 398*: *Extreme Solar Systems*, D. Fischer *et al.*, Eds. (Astronomical Society of the Pacific, San Francisco, 2008), pp. 405–418.
35. I. Baraffe, G. Chabrier, T. Barman, *Astron. Astrophys.* **482**, 315 (2008).
36. E. R. Adams, S. Seager, L. Elkins-Tanton, *Astrophys. J.* **673**, 1160 (2008).
37. The Extrasolar Planets Encyclopedia is available at http://exoplanet.eu.
38. Kepler was competitively selected as the 10th Discovery mission. Funding for this mission is provided by NASA's Science Mission Directorate.

Supporting Online Material

www.sciencemag.org/cgi/content/full/science.1185402/DC1
SOM Text
Fig. S1
References

1 December 2009; accepted 28 December 2009
Published online 5 January 2010;
10.1126/science.1185402
Include this information when citing this paper.

Tuning the Dimensionality of the Heavy Fermion Compound $CeIn_3$

H. Shishido,[1,2] T. Shibauchi,[1] K. Yasu,[1] T. Kato,[1] H. Kontani,[3] T. Terashima,[2] Y. Matsuda[1]*

Condensed-matter systems that are both low-dimensional and strongly interacting often exhibit unusual electronic properties. Strongly correlated electrons with greatly enhanced effective mass are present in heavy fermion compounds, whose electronic structure is essentially three-dimensional. We realized experimentally a two-dimensional heavy fermion system, adjusting the dimensionality in a controllable fashion. Artificial superlattices of the antiferromagnetic heavy fermion compound $CeIn_3$ and the conventional metal $LaIn_3$ were grown epitaxially. By reducing the thickness of the $CeIn_3$ layers, the magnetic order was suppressed and the effective electron mass was further enhanced. Heavy fermions confined to two dimensions display striking deviations from the standard Fermi liquid low-temperature electronic properties, and these are associated with the dimensional tuning of quantum criticality.

Heavy fermion materials are metallic compounds with extremely large effective electron masses, and they typically contain a rare-earth element. In these materials, the electrons populating the 4f orbitals are, at high temperatures, essentially localized with well-defined magnetic moments. As the temperature is lowered, the localized moments are screened by conduction electrons (s, p, and d orbitals), forming a nonmagnetic state by virtue of the Kondo effect (*1*). At yet lower temperatures, the f-orbital electrons dressed by conduction electron clouds (Kondo clouds) become itinerant, forming a very narrow conduction band that is characterized by a heavy effective quasiparticle mass. On the other hand, the Ruderman-Kittel-Kasuya-Yosida (RKKY) interaction, which is an intersite exchange interaction between the localized f-orbital moments, promotes magnetic ordering. Thus, the ground state of these compounds is either a nonmagnetic metal or a magnetically ordered state, as determined by the competition of the above two effects. Generally, in reduced spatial dimensions, many-body correlation effects due to the Coulomb interaction between electrons become more relevant. Moreover, thermal and quantum fluctuations are significantly enhanced, extending critical regimes with no long-range ordering to a wide temperature range. Therefore, many-body effects that are not observed in three dimensions are expected to arise in two-dimensional (2D) heavy fermion systems.

Quantum criticality is a central research issue in the physics of highly correlated matter (*2*, *3*). In conventional metals, interacting electrons (quasiparticles) are well described by Landau's Fermi liquid theory. Near the quantum critical point (QCP), where a second-order phase transition occurs at zero temperature, low-lying spin fluctuations give rise to a serious modification of the quasiparticle mass and the scattering cross section of the Fermi liquid. This results in a strong deviation of physical properties from the standard Fermi liquid behavior. In heavy fermion metals, quantum criticality can be tuned by external parameters, such as doping, pressure, and magnetic fields (*2*). Fabricating superlattice heterostructure provides another way to control the quantum criticality through "dimensional tuning"; however, the epitaxial growth of heavy fermion thin films has been challenging (*4*–*6*).

There have been attempts to realize heavy fermion systems with low dimensions. One is the bulk crystals of $CeTIn_5$ (where T = Rh, Co, or Ir), whose crystal structure yields alternating layers of $CeIn_3$ and TIn_2 (*7*, *8*). However, the largely corrugated Fermi surface (*9*), the small anisotropy of upper critical fields (*10*), and the strong deviations from 2D antiferromagnetic spin fluctuations (*11*) all indicate that the electronic and magnetic properties of $CeTIn_5$ are anisotropic 3D rather than 2D. Another example is the bilayer 2D films of ^{3}He fluid (*12*), where the mass enhancement is observed near a QCP. Here the controlled parameter is the ^{3}He density of the second layer. However, the dimensional tuning from 3D to 2D heavy fermions is still lacking.

The heavy fermion compound $CeIn_3$ appears to be a good candidate for addressing the key issues of QCP physics. Bulk cubic $CeIn_3$ exhibits a 3D antiferromagnetic ordering at Neel temperature T_N = 10 K (*13*, *14*) that is destroyed in a quantum phase transition accessed by applying pressure. Near the critical pressure of $p_c \sim 24$ kbar, in the vicinity of the QCP, $CeIn_3$ undergoes a transition into an unconventional superconducting state, and a remarkable deviation from the Fermi liquid behavior is reported (*14*–*16*). To adjust the dimensionality in a controllable way, we used molecular beam epitaxy to grow the $CeIn_3/LaIn_3$ superlattices (Fig. 1A): m layers of $CeIn_3$ and n layers of isomorphic $LaIn_3$ were grown alternately, forming an (m:n) heterostruc-

[1]Department of Physics, Kyoto University, Kyoto 606-8502, Japan. [2]Research Center for Low Temperature and Materials Sciences, Kyoto University, Kyoto 606-8501, Japan. [3]Department of Physics, Nagoya University, Nagoya 464-8602, Japan.

*To whom correspondence should be addressed. E-mail: matsuda@scphys.kyoto-u.ac.jp